Magnetic-field-driven alteration in capillary filling dynamics in a narrow fluidic channel

Srinivas R. Gorthi, Pranab Kumar Mondal, and Gautam Biswas[*]

Department of Mechanical Engineering, Indian Institute of Technology, Guwahati 781039, India

(Received 26 March 2017; revised manuscript received 18 June 2017; published 21 July 2017)

We investigated pressure-driven transport of an immiscible binary system, constituted by two electrically conducting liquids, in a narrow fluidic channel under the influence of an externally applied magnetic field. The surface wettability was taken into account in the analysis considering that the walls of the channel are chemically treated to obtain various predefined contact angles as required for the study. Alterations in the capillary filling and wetting dynamics in the channel stemming from a complex interplay among different forces acting over the interface were investigated. It was shown that an alteration in the strength of the magnetic field leads to an alteration in the dynamics of the interface, which in turn, alters the filling and wetting dynamics nontrivially upon interaction with the surface tension force due to the wetted walls of the channel. It is emphasized that a contrast in properties of constituents of the binary system gives rise to an alteration in the forces being applied across the interface, leading to an intricate control over the filling and wetting dynamics for a given flow configuration and an applied field strength. We believe that the results obtained from this analysis may aid the design of microfluidic devices used for multiphase transport.

I. INTRODUCTION

The displacement of one fluid by another is ubiquitous in different natural processes such as rainfall on window panes, movement of water droplets over lotus leaves, and tear films on the cornea, to name a few. The movement of immiscible binary fluids also finds many applications in technologically relevant areas. A few important applications include movement of biofluids in lab-on-a-chip devices, on-chip bioanalysis, and filling in physiological systems during artificial grafting [1–4]. In view of the numerous applications of immiscible binary fluids in miniaturized systems and devices along with a need for the systematic investigation of different aspects of the underlying interfacial flow characteristics, researchers have recently concentrated on the microscale transport of immiscible binary systems [5–9]. The control over filling of an immiscible system in narrow fluidic pathways, relevant in many areas from biomedical and biochemical processes to cooling in microelectromechanical systems (MEMS), is one of the challenging tasks in the domain of microscale transport [10–12]. When a two-fluid system moves in a narrow fluidic channel, the interfacial transport plays a major role and affects the filling rate in the channel entailing the dynamics of the contact line formed at the fluid–fluid–solid interface changed. It should be mentioned that although alterations in the dynamics of contact line motion, triggered by several factors such as imposition of surface structuring over solid substrates or modulation of the wetting characteristics of the surface, give rise to an overall change in the interfacial dynamics, the ultimate consequence of which is largely reflected in the filling rate and its control in the fluidic system [10–14].

It is important to mention that active control of the filling rate in the context of microscale transport is far from trivial, thus necessitating alternative means of implementation to achieve control in microflows. Paying careful attention to this aspect, researchers have explored different avenues such as surface modifications, viz., artificial texturing of the surface, decoration of the surface with patterned wettability gradients, and alterations to the flow actuation mechanism with the aim of realizing better controllability of microscale and nanoscale transport [10,11,13,15–17]. In all cases mentioned above, the motion of the contact line formed between a pair of immiscible fluids is altered as a result of the extensive interplay among the dominating forcing factors, leading to alterations in the filling and wetting dynamics. When employing electroosmotic effects or thermocapillary actuation in realizing microscale multiphase transport, greater maneuverability of the filling rate can be achieved, as reported in the literature [6,18,19]. In contrast, application of a magnetic field in microscale transport has attracted attention as it offers precise controllability of the flow rate in the context of single-phase transport [20–22]. An applied magnetic field gives rise to a body force acting on the fluid mass, which also depends on the electrical conductivity of the fluid, upon interacting with the flow velocity has a forcing effect on the fluid mass, thus interfering with the fluid motion in the process [20,22–24]. Such a paradigm, however, could be extended to alter the interfacial dynamics of transport of an immiscible binary system over a wetted surface, solely by altering the forces acting across the contact line formed at the fluid–fluid–solid interface. It may be mentioned in this context that the underlying physical considerations are nontrivial, because of the intricate nonlinear interactions among different forces stemming from the viscous drag, surface tension effect as modulated by the wettability of the surface, and the Lorentz force due to the applied magnetic field. Although studies are in progress with the aim of achieving finer control in microscale and nanoscale transport, e.g., surface modifications by altering the physicochemical properties of the surface [10,11,25,26], by surface structuring [7,10,27,28], from the presence of nanobubbles over a hydrophobic surface [17,29], and by altering the flow actuation parameters [6,19,30]. There are better prospects in applying magnetic field-induced forcing to provide effective control of the capillary filling rate, not reported so far. The earlier work [30] is augmented in the current investigation with a view to understand the dynamics

---

[*]gtm@iitg.ernet.in

013113-1

of the interface under the influence of magnetic field. It is also envisaged that the dynamics of the interface influence the dynamics of the contact line.

In this work, we investigated the capillary transport of an immiscible binary system constituted by a pair of conducting liquids, under the influence of an applied magnetic field in a narrow fluidic channel. We investigated alterations in the interfacial dynamics and their consequential effects on the capillary filling and wetting dynamics in the channel, stemming from a complex interplay among the magnetic field-induced forcing, the surface tension force originating from the surface wettability, and the viscous drag. The magnetic field-induced forces acting over the multiple phases depend substantially on the electrical conductivity of the respective phases, while changes in the viscosity ratio between the phases will result in different magnitudes of viscous drag in the binary system during transit through the channel. The underlying physical aspects of microscale multiphase transport with contrasting properties in the presence of an applied magnetic field, which could lead to even more complex dynamics which were not reported earlier, have been investigated through numerical simulations. We believe that the analysis carried out in this work will provide fundamental insights towards improving the design of microfluidic systems and devices widely used for transport of immiscible fluids typically in medical diagnostics and on-chip bioanalysis.

II. COMPUTATIONAL DOMAIN SETUP

A. Formulation of the problem

We consider the pressure-driven transport of a binary fluid system through a narrow fluidic channel of length L and height $2H$ formed between two parallel plates, under the influence of an applied magnetic field as shown schematically in Fig. 1. The coordinate system is attached to the channel, the x axis along the channel length and the y axis is the vertical axis along channel height. We consider that the channel dimension in the third dimension is significantly larger than the channel height, which, in essence, allows us to consider a two-dimensional flow scenario. The binary system is constituted by two immiscible components, viz., fluid A (advancing phase liquid; shown in pink) and fluid
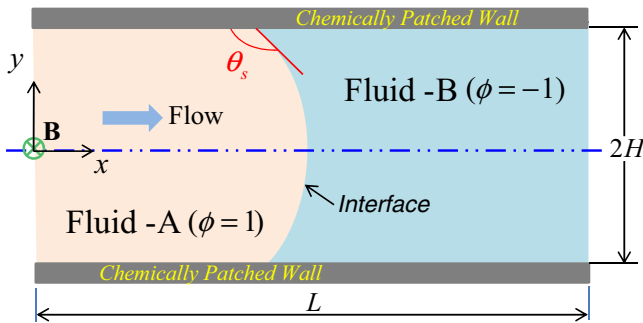

FIG. 1. Schematic illustrating the interface of two fluids where fluid A is displacing fluid B in a confined channel whose walls have surface wettability. The height and length of the channel are L and $2H$ respectively. Magnetic field of strength $\mathbf{B}(= B\hat{k})$ is applied along z direction of the channel (perpendicular to the plane of the paper).

B (receding phase liquid; shown in blue). In this analysis, we consider that both fluids are Newtonian and they are also electrically conducting. We further consider that the walls of the channel are uniformly coated with a suitable chemical that permits a predefined contact angle. Thus, the walls are chemically homogeneous throughout the length of the channel. We use the diffuse interface phase-field framework to track the spatiotemporal evolution of interface formed between two immiscible Newtonian fluids confined between two solid surfaces as shown in Fig. 1. The flow field is described by the Navier–Stokes system of equations taking the effects of the capillary stress and also the magnetic force into account. We next discuss the transport equations and their boundary conditions in detail.

B. Phase-field model

The diffuse interface framework of the phase-field model employs an order parameter $\phi(\mathbf{r},t)$, known as the phase-field parameter, to describe at any instant the state of a system having two immiscible phases. The phase-field parameter is defined as the normalized phase concentrations of the respective phases. We define the order parameter as $\phi = (n_1 - n_2)/(n_1 + n_2)$, where, n_1 and n_2 are the number-density of molecules of fluid A and fluid B, respectively. Hence the advancing phase fluid (fluid A) is defined by $\phi = 1$, while $\phi = -1$ indicates the receding phase fluid (fluid B). However, the interface separating the phases can be described by $\phi \in (-1,1)$. The Ginzburg–Landau free-energy functional of the system as considered in the present analysis can be expressed as [31–33]

$$F(\phi) = \int_{\Omega} \left[f(\phi) + \frac{\sigma \xi}{2} |\nabla \phi|^2 \right] d\Omega, \quad (1)$$

where Ω is the entire volume and σ and ξ are the surface tension coefficient and the thickness of the interfacial region, respectively. The first term on the right-hand side of Eq. (1) denotes the free-energy density of the system in the bulk, and the second term represents the finite valued free-energy density of the diffuse interface separating the bulk phases. Further, the bulk free-energy density $f(\phi)$ is described by a double-well structure and has the form $f(\phi) = \sigma(\phi^2 - 1)^2/4\xi$ and exhibits two minima ($\phi = \pm 1$), corresponding to the two stable phases, fluids A and B, of the present system. The minimization of the free energy of the system as given in Eq. (1) along with the mass conservation of the respective phases leads to the well-known Cahn–Hilliard equation, which governs the dynamic evolution of the phase-field parameter ϕ. The Cahn–Hilliard equation, which is the convection–diffusion equation of the phase-field variable, can be written as follows [34,35]:

$$\phi_t + \mathbf{v} \cdot \nabla \phi = \nabla \cdot (M \nabla G), \quad (2)$$

where M is the mobility parameter of the phase-field variable, $M = M_c(1 - \gamma \phi^2)$, where the parameter γ controls the interface dynamics of the two-phase system, and M_c is the critical mobility parameter [32,36]. The term on the right-hand side of Eq. (2) represents the diffusion of the phase-field parameter. Continuous diffusion of the phase-field variable ϕ across the interface leads to the removal of stress singularity arising at the three-phase (fluid–fluid–solid) contact line. The term G on the right-hand side of Eq. (2) is the chemical potential, which

is defined by the variational derivative of the free energy of the system and can be written as

$$G = \delta F/\delta\phi = \partial f/\partial\phi - \sigma\xi(\nabla^2\phi)$$
$$= \{\sigma[(\phi^3 - \phi) - \xi^2\nabla^2\phi]/\xi\} \quad (3)$$

We discuss here the boundary conditions for the phase-field equation. Ensuring no flux across the bounding solid substrate and also to specify the wetting condition of the surface, we use the following conditions on the solid surface for the transport equation of the phase-field variable [37]:

$$\nabla G \cdot \mathbf{n} = 0, \quad (4a)$$

$$\mathbf{n} \cdot \nabla\phi = -\tan\left(\frac{\pi}{2} - \theta_s\right)|\nabla\phi - (\mathbf{n} \cdot \nabla\phi)\mathbf{n}|, \quad (4b)$$

where θ_s is the static contact angle specified on the walls of the channel and $\mathbf{n}$ is the unit normal pointing outwards from the walls. It is worth mentioning that Eq. (4a) confirms no flux through the surface, while the condition given in Eq. (4b), which is also known as the geometric boundary condition [37], maintains the order parameter profile at the three-phase contact line according to the contact angle θ_s specified at the solid surface [37].

C. Transport equations for the system

The Navier–Stokes equations in their dimensional form, for an incompressible Newtonian fluid including different forcing terms originating from the contribution of the phase-field parameter and applied magnetic field [12,30,38] are given as

$$\rho_i(\mathbf{u}_t + \mathbf{u} \cdot \nabla\mathbf{u}) = -\nabla p + \nabla \cdot [\mu_i(\nabla\mathbf{u} + \nabla\mathbf{u}^T)]$$
$$+ G\nabla\phi + \mathbf{F}_{\text{Mag}}, \quad (5a)$$

$$\nabla \cdot \mathbf{u} = 0. \quad (5b)$$

Equations (5a) and (5b) govern the fluid flow in the channel, where $\mathbf{u}$ is the velocity vector, p is the pressure, and

ρ_i and μ_i denote the density and viscosity of the ith-phase fluid, where $i = A, B$ are the two phases. The first two terms on the right-hand side of Eq. (5a) are the contributions from the hydrodynamic stress. The penultimate term is the capillary force density and acts only at the interfacial region. The flow field-induced local change of the interface curvature multiplied by the surface tension gives rise to an additional body force term $G\nabla\phi$ in the momentum balance equation due to presence of participating phases (see the Appendix). The last term in Eq. (5a) is another body force known as the Lorentz force and represents the effect of the applied magnetic field on the flow dynamics. In this analysis, we consider a constant applied magnetic field to determine its effect on the underlying interfacial transport. We can write, in dimensional form, the expression for the induced Lorentz force term as [20]

$$\mathbf{F}_{\text{Mag}} = \varepsilon(\mathbf{E} + \mathbf{u} \times \mathbf{B}) \times \mathbf{B}, \quad (6)$$

where ε is the electrical conductivity. Since no external electric field is applied, the polarization voltage is also neglected here. We can therefore consider $\mathbf{E} = \mathbf{0}$ [38]. In this situation, the Lorentz force reduces to

$$\mathbf{F}_{\text{Mag}} = \varepsilon(\mathbf{u} \times \mathbf{B}) \times \mathbf{B}. \quad (7)$$

We further consider that, as the case may be for partially ionized fluids or metallic liquids, the values of the magnetic Reynolds number, $\text{Re}_m = u_{\text{ref}} l_{\text{ref}}/\mu_e$, and the magnetic Prandtl number, $\text{Pr}_m = v/\mu_e$ are very small ($\ll 1$) [20]. The terms u_{ref} and l_{ref} are the typical velocity and length scales respectively. μ_e and v are the magnetic diffusivity and kinematic viscosity of the fluid, respectively. The above considerations, in essence, allow us to ignore the induced magnetic field produced by the motion of an electrically conducting fluid in the present analysis. Also, for solving the Navier–Stokes equation, we consider the following boundary and initial conditions:

$$\begin{array}{ll} \text{Initial condition:} & \mathbf{u}(\mathbf{r}, t = 0) = \mathbf{0} \ \forall \ \mathbf{r} \\ \text{Boundary conditions:} & \begin{cases} u, v = 0; & \text{at the channel walls} \\ u = u_{\text{in}}; & \text{at the channel inlet} \\ p_{\text{gauge}} = 0; & \text{at the channel outlet} \end{cases} \end{array} \right\}. \quad (8)$$

At the inlet of the channel (left boundary), following the same profile as used in the literature [36], we consider the velocity inlet boundary condition:

$$u_{\text{in}} = 6u_{\text{avg}}(y/H)[1 - (yH)]. \quad (9)$$

D. Nondimensionalization of transport equations

Nondimensional form of transport equations were utilized for numerical simulations of the two-phase system using the following scales: length scale, $l_{\text{ref}}(= 2H)$; characteristic velocity scale, $u_{\text{ref}}(= u_{\text{avg}})$; characteristic time scale, $t_{\text{ref}}(= l_{\text{ref}}/u_{\text{ref}})$, pressure scale, $p_{\text{ref}} = \mu_{\text{ref}} u_{\text{ref}}/l_{\text{ref}}^2$; and characteristic scale of the order parameter, $\phi_{\text{ref}} = (|\phi_\pm| = 1)$. We then have the

following nondimensional equations:

$$\bar{\phi}_{\bar{t}} + \bar{\mathbf{u}} \cdot \bar{\nabla}\bar{\phi} = \frac{1}{\text{PeCn}}\bar{\nabla} \cdot (\bar{M}\bar{\nabla}\bar{G}), \quad (10)$$

$$\text{Re}\bar{\rho}(\bar{\mathbf{u}}_{\bar{t}} + \bar{\mathbf{u}} \cdot \bar{\nabla}\bar{\mathbf{u}}) = -\bar{\nabla}\bar{p} + \bar{\nabla} \cdot \bar{\mu}[(\bar{\nabla}\bar{\mathbf{u}}) + (\bar{\nabla}\bar{\mathbf{u}})^T]$$
$$+ \frac{1}{\text{CaCn}}\bar{G}\bar{\nabla}\bar{\phi} + \bar{\mathbf{F}}_{\text{Mag}}, \quad (11)$$

$$\bar{\nabla} \cdot \bar{\mathbf{u}} = 0, \quad (12)$$

where symbols with overbars are dimensionless quantities, $\bar{\rho}(= \rho/\rho_{\text{ref}})$ and $\bar{\mu}(= \mu/\mu_{\text{ref}})$ in Eq. (11) are the effective phase-averaged mass density and the effective viscosity, respectively, and $\bar{M}(= M/M_c) = (1 - \gamma\phi^2)$ is the dimensionless mobility parameter, where γ has been defined

earlier. We consider the case where $\gamma = 0$ such that $\bar{M} = 1$ [30,32,36]. Another important point here is that, following the reported MD simulation studies [5], the critical mobility parameter M_c is defined as $M_c = Cl^4/\sqrt{m\varepsilon_e}$, where l and ε_e are the length scale and energy scale, respectively, in the Lennard-Jones potential for fluid molecules, m is the molecular mass of the fluid, and C is a constant (~ 0.023).

We assume that a uniform magnetic field of strength B_o is acting in the direction parallel to the z-direction, i.e., perpendicular to the plane of the paper, which then leads to the following expression of the Lorentz force acting on the electrically conducting binary system as already taken into account in Eq. (11). The dimensionless Lorentz force can be expressed as

$$\bar{\mathbf{F}}_{\text{Mag}} = -\bar{\varepsilon}\text{Ha}^2\bar{\mathbf{u}}, \tag{13}$$

where $\bar{\varepsilon}$ is the phase-averaged electrical conductivity of the binary system. Equations (10), (11), and (13) contain some dimensionless parameters elucidated as follows:

Peclet number: $\text{Pe} = \frac{u_{\text{ref}}l_{\text{ref}}}{M_c}$, which is the ratio of l_{ref} to the diffusion length M_c/u_{ref};

Reynolds number: $\text{Re} = \frac{\rho_{\text{ref}}u_{\text{ref}}l_{\text{ref}}}{\mu_{\text{ref}}}$, which is the ratio of inertia and viscous forces;

Capillary number: $\text{Ca} = \frac{\mu_{\text{ref}}u_{\text{ref}}}{\sigma}$, which is the relative strength between viscous and surface tension forces;

Cahn number: $\text{Cn} = \frac{\xi}{l_{\text{ref}}}$, which represents the ratio of interface thickness to the height of the channel.

Hartmann number: $\text{Ha} = \sqrt{\frac{\varepsilon_{\text{ref}}B_0^2 l_{\text{ref}}^2}{\mu_{\text{ref}}}}$, which represents the relative strength between the magnetic and viscous forces.

As mentioned earlier, the phase-averaged properties of the two-fluid system can be a linear function of the order parameter ϕ:

$$\rho = \frac{(\phi + 1)(\rho_A - \rho_B) + 2\rho_B}{2}, \tag{14a}$$

$$\mu = \frac{(\phi + 1)(\eta_A - \eta_B) + 2\mu_B}{2}, \tag{14b}$$

$$\varepsilon = \frac{(\phi + 1)(\varepsilon_A - \varepsilon_B) + 2\varepsilon_B}{2}. \tag{14c}$$

In this context it should be mentioned that in two-phase configurations, the fluid properties of either of the fluids can be chosen as the reference properties. However, in the present analysis, we consider the properties of the advancing phase fluid (fluid A) as the reference values [36,39,40]. Hence, the expression for the dimensionless phase-averaged properties appearing in Eqs. (11) and (13) can be further written as

$$\bar{\rho} = \frac{(\phi + 1)(1 - \rho_r) + 2\rho_r}{2}, \tag{15a}$$

$$\bar{\mu} = \frac{(\phi + 1)(1 - \eta_r) + 2\mu_r}{2}, \tag{15b}$$

$$\bar{\varepsilon} = \frac{(\phi + 1)(1 - \varepsilon_r) + 2\varepsilon_r}{2}, \tag{15c}$$

where $\rho_r(= \rho_B/\rho_A)$, $\mu_r(= \mu_B/\mu_A)$, and $\varepsilon_r(= \varepsilon_B/\varepsilon_A)$ are the density ratio, viscosity ratio, and electrical conductivity ratio, respectively, of the binary fluid system considered in this study. To take the effect of surface wettability into account in this
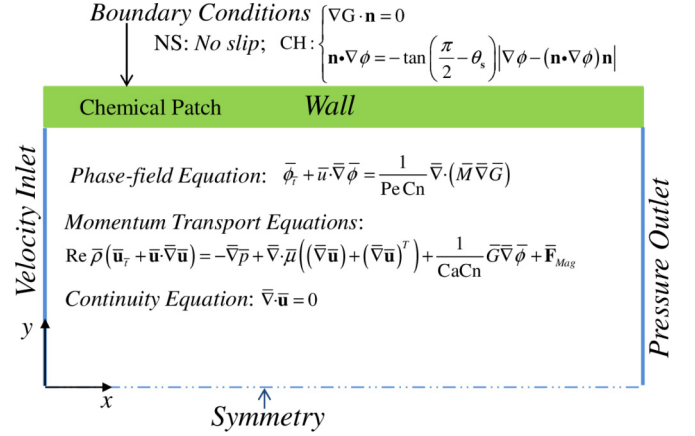

FIG. 2. Schematic of the computational domain showing the governing equations and the boundary conditions. The axes are placed at the left center of the channel. We consider the symmetry half of the channel for numerical simulations owing to the symmetric nature of the flow with respect to the channel center.

analysis, we consider different static contact angle θ_s values, which are specified at the walls of the channel.

E. Numerical approach and model validation

We use the finite-element framework of COMSOL to solve the coupled phase-field–Navier–Stokes system of equations. Figure 2 depicts schematically the computational domain, which shows the governing transport equations along with the boundary conditions in their dimensionless form. For all the numerical simulations, the PARDISO solver with the generalized-α scheme of COMSOL multiphysics was used for the time-stepping. The initialization of the phase-field variable was performed before allowing bulk fluid motion. Initialization of the phase-field variable leads to an equilibrium interface profile of the two coexisting bulk phases ($\phi = 1, -1$) following the solution of the equation, $\mu(\phi) = 0$, while the equilibrium order parameter profile normal to the plane interface is given by [8,32]

$$\phi(\bar{z}) = \tanh(\bar{z}/\sqrt{2}\xi), \tag{17}$$

where $\bar{z}$ is the coordinate direction normal to the plane interface. It may be noted that it is analogous to coordinate x in present work (see Fig. 1).

1. Model benchmarking

Here we attempt to benchmark the present numerical framework with the results reported in the literature in the area of multiphase microscale transport. We validate the diffuse interface framework of the numerical method employed in this study with the results reported by Yue *et al.* [12]. We consider a 2D rectangular channel having height W and length 4W while validating our model. The top and bottom walls are moving with the same constant velocity but in opposite directions. Figure 3 shows the liquid–liquid interface in the steady state for values of the other parameters of Re = 0.001 and Cn = 0.02. The value of the Peclet number is taken as Pe = CaCn/S^2, where $S = 0.01$ is the diffusion length scale [12]. Here we consider triangular grids of size $\Delta x, \Delta y = \text{Cn}/2$.

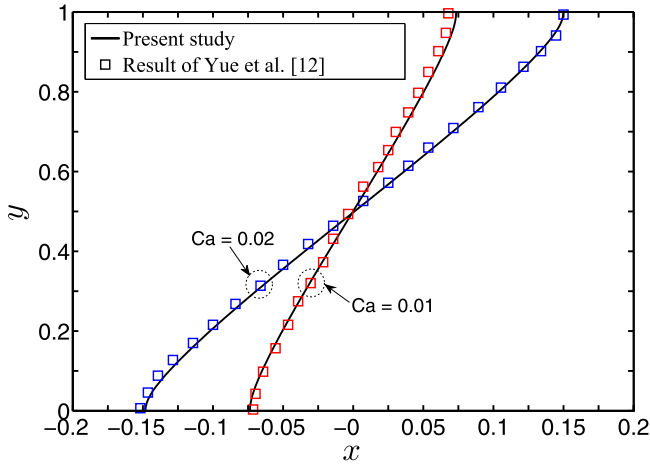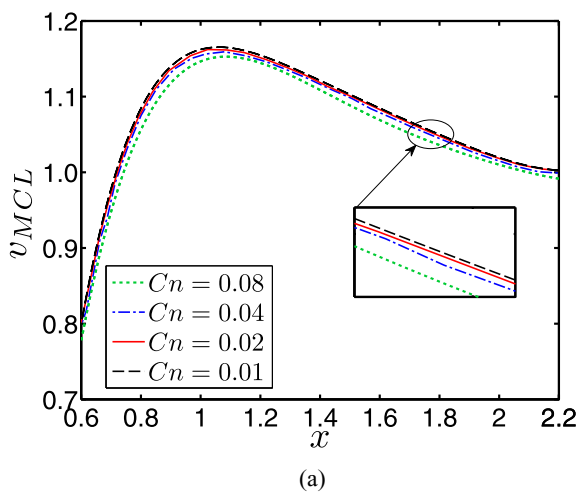FIG. 3. Model benchmarking: interface deformation for different values of Ca. The other parameters are $\text{Re} = 0.001, \text{Cn} = 0.02, \text{Ha} = 1$, and $\theta_s = 90°$. The value of the Peclet number is taken as $\text{Pe} = \text{CaCn}/S^2$, where $S = 0.01$ and represents the diffusion length scale [12]. The results reported by Yue *et al.* [12] are shown by symbols of different shades, and the solid line represents the results obtained from the present numerical framework. The variations obtained from the present study match well with the results reported in Ref. [12].
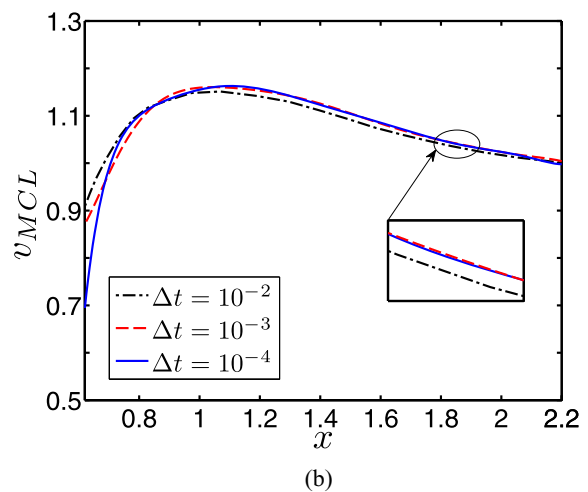
It can be seen from Fig. 3 that the results obtained from the present modeling framework show a good match with reference.

2. Grid convergence analysis

To capture the underlying flow physics for the problem considered in this analysis, we require relatively finer grid sizes consistent with the physical problem. Since the Cahn number (Cn) defines the physical size of the grid, we perform simulations for a given case, considering different values of Cn to ensure that the results reported in this study are independent

of grid resolution. To be precise, we depict in Fig. 4(a) the variation of the contact-line velocity obtained at different Cn. We find an insignificant change in the results when Cn varies from 0.08 to 0.01. While Cn = 0.01 represents a very fine grid which would be computationally intensive, Cn = 0.04 is the sharp interface limit as proposed in Ref. [12]. Hence, we considered Cn = 0.02 for all the simulations in the present study.

It is worth mentioning that the value Cn = $0.02(\sim 10^{-2})$ as chosen in this analysis makes the grid resolution sufficient to obtain physically meaningful and converged solutions, while also maintaining the sharp interface limit [12]. Note that this value of Cn = 0.02 even falls well below its threshold limit as proposed in Ref. [12], i.e., Cn = 4S, where S = 0.01, from the perspective of attaining a sharp interface limit. Also, it should be mentioned that the parameter S (= 0.01) as defined in Ref. [12] is equivalent to the Peclet number (Pe) as considered in this study.

One may further note from Fig. 4(b) that the velocity of the contact line only beyond $x = 0.8$ has been considered to exclude initial effects after admittance of fluid-A into the channel. However, the flow still remains in the transient regime before reaching the steady state. It may be observed that the variation in velocity becomes insignificant as the time step size Δt changes from 10^{-3} to 10^{-4}. Hence, we consider $\Delta t = 10^{-3}$ as the time step throughout this study. It is also mentioned that value of Hartmann number Ha = 1, implying that the magnetic field strength **B** is nonzero in the model benchmarking and grid convergence studies.

III. RESULTS AND DISCUSSION

In the present study, we consider two immiscible fluids flowing in a microcapillary over a surface having predefined wettability as manifested in terms of the static contact angle θ_s. In our numerical computations, we consider a channel length of $[\bar{L} = 4 \times (2\bar{H})]$, where $\bar{H}$ is the half-height of the channel. Owing to the symmetric nature of the flow dynamics about
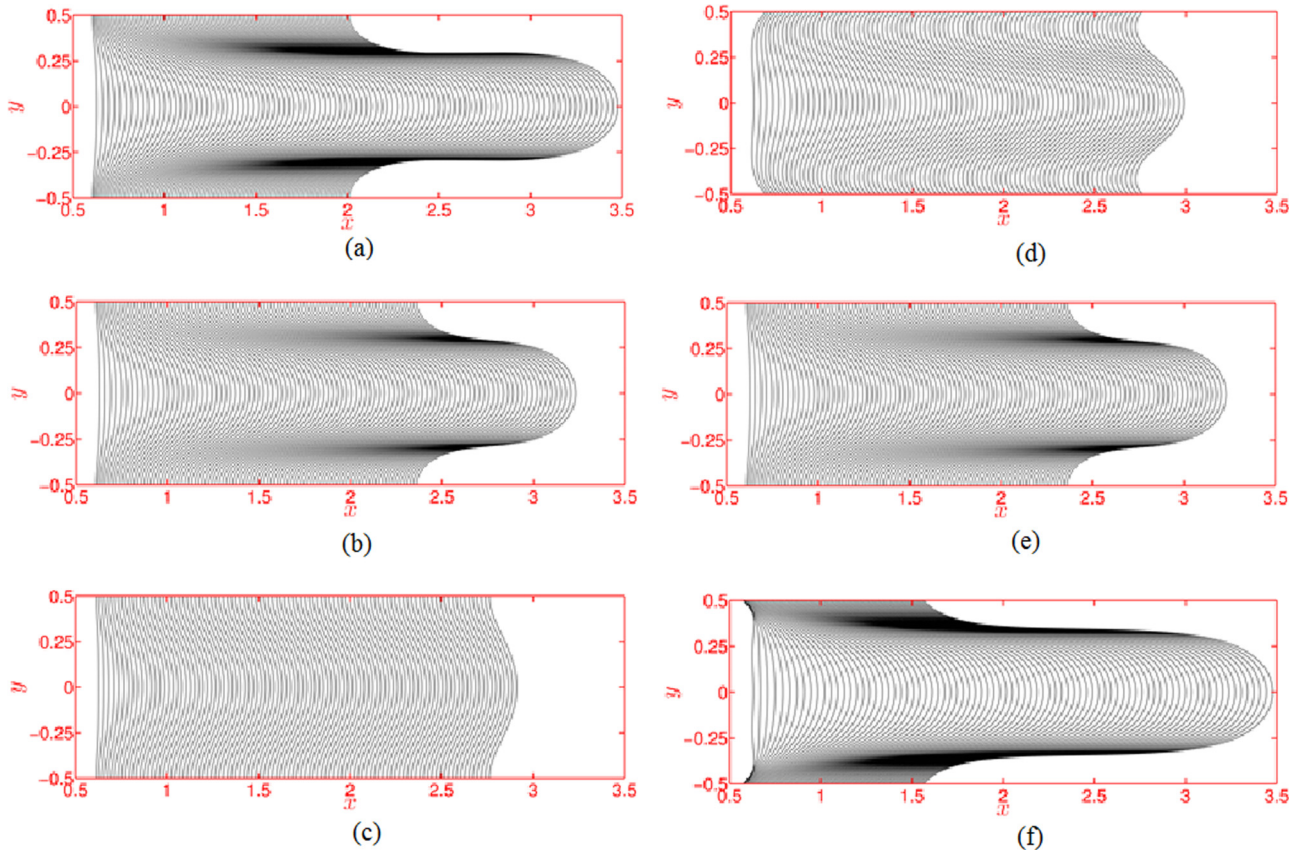

(a)

(b)

FIG. 4. (a) Variation showing the grid independence results for the present study. Since the grid sizes depend on the value of Cn, we clearly illustrate the variation of the contact-line velocity v_{MCL} with x for different Cahn numbers (Cn) with Re = 0.03, Ca = 0.08, Ha = 1, and $\theta_s = 90°$. The results become independent as Cn varies from 0.02 to 0.08. (b) The independence of the time step size is shown by plotting the variation of the contact-line velocity v_{MCL} with x for different Δt resolutions with Re = 0.03, Ca = 0.08, Ha = 1, and $\theta_s = 90°$. The change in velocity becomes insignificant as Δt changes from 10^{-3} to 10^{-4}.

FIG. 5. Plot depicting the interface evolution inside the channel: (a) $Ha = 0.1$, (b) $Ha = 1$, (c) $Ha = 10$, (d) $\theta_s = 45°$, (e) $\theta_s = 90°$, and (f) $\theta_s = 135°$. The other parameter for (a)–(c) is $\theta_s = 90°$ and for (d)–(f), $Ha = 1$, and in all cases $Pe = 0.2$, $Ca = 0.08$, and $Re = 0.03$. The figure shows the two different kinds of interface profiles: commodious profiles and crowding interface profiles. The formation of crowding interface profiles leads to "fingerlike" dynamics.

the channel center ($y = 0$), we consider the symmetry half of the domain for our numerical experiments. We discuss here the interfacial magnetohydrodynamics for two different cases. First, we consider the ratios of all the properties of the fluids viz., the density, viscosity, and electrical conductivity, to be unity. Second, we look at the effect of contrasting properties of the binary fluid system on the underlying interfacial transport. In addition to those mentioned above, the other parameters considered, unless specified otherwise, for this analysis are $Pe = 0.2$, $Ca = 0.08$, $Re = 0.03$, and $Ha \in (0.1,10)$. Note that the chosen values of the different dimensionless parameters in this analysis are in accord with those typically used in microscale transport [25,36,38]. Since the prime focus of the present endeavor is look into the capillary filling dynamics, which largely depends upon the spatiotemporal evolution of the interface in the channel, we start our discussion with a diagram depicting the time sequence plots of the interface for different cases as discussed in the forthcoming paragraph. It should be noted that from here onwards, for clarity of presentation, we do not use an overbar above symbols to represent dimensionless quantities.

A. Interfacial dynamics of a property-matched binary system

1. Evolution of the interface

Figures 5(a)–5(f) show the time sequences of the interface profiles for the different cases considered in this analysis. Note

that these time sequences are the loci of the points having a value of the order parameter $\phi = 0$ with position obtained at different time. Figures 5(a)–5(c) depict the interface profiles for three different values of Ha ($= 0.1$, 1, and 10), the other parameters being $\theta_s = 90°$, $Pe = 0.2$, and $Ca = 0.08$. Figures 5(d)–5(f) were obtained by considering $Ha = 1$ and for three different contact angles, $\theta_s = 45°$, $90°$, and $135°$, respectively. Figure 5(a) indicates that, for smaller Ha (0.1), the progression of the advancing fluid front inside the capillary is mainly affected by the applied pressure gradient and the surface tension force. Since for $Ha = 0.1$ the retardation of the interface at the channel center is relatively less, for a given case of $\theta_s = 90°$, the pressure force, which is acting over the complete lateral extent of the interface, will attempt to severely stretch the interface at the middle. More precisely, a relatively higher velocity of the interface at the middle part of the channel will lead to a slower movement of the contact line following the mass conservation effect in the advancing fluid phase. Note that the slower movement of the contact line is also favored by the relative smaller value of Ha (0.1) (the net force on the contact line is less for $Ha = 0.1$). These two forcing factors bring about a relative motion of the interface between the contact line and the central part, leading to "fingerlike" dynamics of the front as seen in Fig. 5(a).

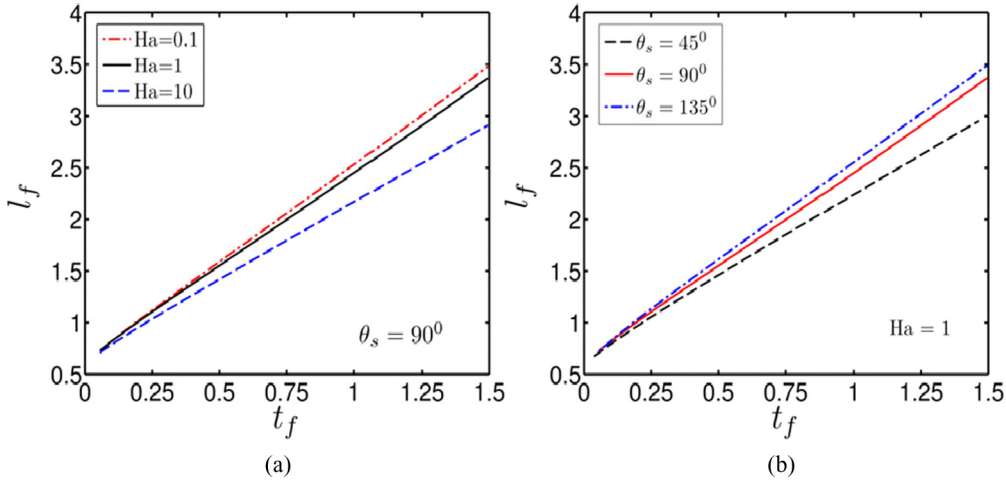With increasing magnitude of Ha, since the contact line motion is largely affected by the induced Lorentz force, the

FIG. 6. Variation of capillary filling length (l_f) with filling time (t_f): (a) for different values of Ha = 0.1, 1, and 10, obtained at $\theta_s = 90°$; (b) for different values of $\theta_s = 45°$, 90°, and 135°, obtained at Ha = 1. Other parameters were taken as follows: Pe = 0.2, Ca = 0.08, and Re = 0.03. The filling time, for a given $\theta_s = 90°$ increases with increasing value of Ha; on the other hand, with increasing contact angle, the filling time also decreases.

contact line velocity increases by enjoying a relatively larger net force at the contact line [the effective drag is less; see Fig. 8(b)]. Note that the magnetic force being applied on the interface is proportional to the velocity [see Eq. (13)]. Thus, for a higher Ha the retardation of the interface at the center of the channel becomes higher since the velocity of the interface is always higher at the central part of the channel. These two cumulative effects, in essence, allow the central part of the interface to be retarded more and the "fingerlike" dynamics of the front disappear. The complex dynamics of the interface eventually leads to a decrease in filling time and an increase in wetting time, as discussed in Figs. 6 and 7. The crowding interface profiles as seen in Fig. 5(a) will lead to a relatively lower velocity of the contact line for Ha = 0.1, whereas the commodious interface profiles for Ha = 10 will expedite the movement of the contact line as confirmed in Fig. 5(c). It is important to mention here that the variation of the contact line velocity has been discussed in a subsequent section.

Figures 5(d)–5(f) are merely the time sequence plots of the interface for different values of contact angle $\theta_s = 45°$, 90°, and 135°, respectively, and Ha = 1 in all cases. Figure 5(d) illustrates that, for $\theta_s = 45°$, the interface profiles are not crowded near the contact line, whereas the interface profiles show crowding for $\theta_s = 135°$ although all other parameters remain unaltered. We attribute this observation to the effect of the capillary force density, stemming from the variations in the static contact angle. Since for the surface wettability with $\theta_s = 135°$ the surface tension force restricts the movement of the contact line, the interface profiles become denser near the contact line. This mismatch in the movement of the different parts of the interface (interface at the contact line and at the middle of the channel) induces cooperative–correlative motion of the interface, leading to "fingerlike" dynamics of the front even for a viscosity-matched binary system. In fact, the restricted movement of the interface at the contact line results in relatively greater progress of the advancing liquid
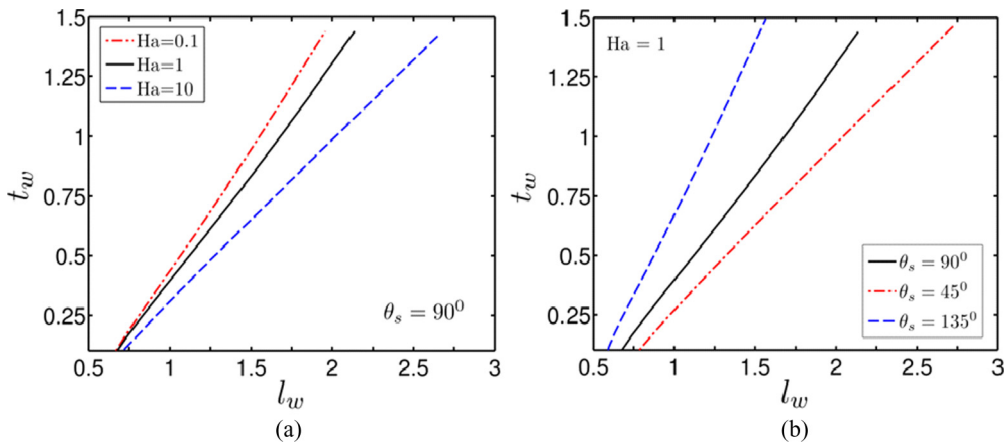

FIG. 7. Variation of capillary wetting length (l_w) with wetting time (t_w): (a) for different values of Ha = 0.1, 1, and 10, obtained at $\theta_s = 90°$; (b) for different values of $\theta_s = 45°$, 90°, and 135°, obtained at Ha = 1. Other parameters were taken as follows: Pe = 0.2, Ca = 0.08, and Re = 0.03. The wetting time, for a given $\theta_s = 90°$, increases with decreasing value of Ha; on the other hand, with increasing contact angle, the wetting time also decreases.

front along the central part of the capillary, thereby promoting the capillary filling rate. It should be mentioned in this context that the spatiotemporal evolution of the interface as modulated by the magnetic force driven alteration in the movement of the interface in the center of the channel as well as the surface tension driven alteration in the contact line velocity may bring in a control over the effective filling and wetting phenomena. In particular, through the time sequence plot of the interface contours, we reconfirm our observations on the filling and wetting dynamics as described in Figs. 6 and 7.

2. Capillary filling dynamics

Capillary filling time is the time required for the advancing phase fluid (fluid A in this study) to infiltrate into the middle part of the capillary under different forcing environments as considered in this analysis. Figure 6(a) shows the temporal variation of the length of the advancing liquid column (l_f) inside the capillary for different values of Ha = 0.1, 1, and 10, obtained at $\theta_s = 90°$. Figure 6(a) shows that, with increasing value of Ha, the length of the advancing fluid front takes a relatively longer time to penetrate a given distance of the channel. Note that the surface wettability ($\theta_s = 90°$) considered for Fig. 6 does not have any preferential attraction toward either of the fluids chosen in this analysis. Another important observation from Fig. 6(a) is that, for $\theta_s = 90°$, the difference in filling time becomes significant as Ha changes from 1 to 10. We attribute this observation to the alteration in the interfacial dynamics of contact line motion as modulated by the applied magnetic field. The motion of the contact line formed at the fluid–fluid–solid interface plays an important role in dictating the interfacial dynamics in microscale transport, which, in turn, lead to the overall modifications in the underlying flow dynamics. Since we have considered the applied magnetic field in the z direction of the channel, the body force due the applied magnetic field affects both momentum equations. Although the filling time is changed with the variation in Ha, the effect of Ha on the filling rate is not linear, and we will discuss this issue in detail later, while concentrating on the dynamics of contact line motion. With increase in Ha, the magnetic field-induced body forces being applied at the interface aid in the forward motion of the contact line, leading to an increment in the contact line velocity. The enhancement of the contact line velocity with increasing value of Ha is shown in Fig. 8(a). To be precise, the consequential effect of the reduction in the advancement of the interface at the middle of the channel increases the contact line velocity, taking into account the effect of mass conservation in the flow field. The middle part of the interface starts to recede at a relatively higher value of Ha leading to an increase in filling time as seen in Fig. 6(a).

In an effort to establish the role of substrate wettability under the influence of magnetic field-driven filling dynamics, Fig. 6(b) compares the length of the advancing fluid front for different wetting conditions of the solid substrate as manifested in terms of the static contact angle θ_s. We observe that, for surface wettability consistent with $\theta_s = 45°$, which also has a preferential attraction toward the advancing phase fluid (fluid A), the time required by the advancing fluid to move through a certain length of the capillary increases, whereas for the cases with $\theta_s = 135°$ the required time decreases. This observation

can be explained as follows: for $\theta_s = 45°$, the surface tension force, which goes in favor of the advancing phase, accelerates the contact line motion. The Lorentz force decelerates the movement of the interface at the middle. The above-mentioned effects and the compliance of continuity equation, results in a larger filling time, as confirmed in Fig. 6(b). In contrast, the surface tension force corresponding to $\theta_s = 135°$ (which acts against the advancing phase) allows the interface to be protruded at the middle, entailing a faster filling rate. We have verified the decrease in contact line velocity for $\theta_s = 135°$ as described later. Figure 6(b) also depicts the filling time for $\theta_s = 90°$. The time required by the interface to fill a given distance along the capillary for a window of contact angle $\theta_s = [45°, 135°]$ is not symmetrical about the same as that attained for $\theta_s = 90°$, largely attributed to the effect of magnetic force on the underlying transport.

3. Capillary wetting dynamics

We refer to the capillary wetting time as the temporal advancement of the advancing phase liquid along the wetted solid substrate. Having established the effect of Ha and surface wettability on the capillary filling dynamics, we proceed to examine the same effects in dictating the capillary wetting phenomena. To do so, in Figs. 7(a) and 7(b) we compare the length of the advancing liquid column along the wetted surface (l_w) plotted as a function of time for different values of Ha and static contact angle θ_s. It can be seen from Figs. 7(a) and 7(b) that the wetting time increases for a relatively smaller value of Ha and a higher value of the contact angle ($\theta_s > 90°$), differing from the temporal variation of filling length as depicted in Figs. 6(a) and 6(b). Note that the capillary wetting length is a direct measure of the velocity of the contact line formed at the fluid–fluid–solid interface. In fact, the wetting as reflected in Figs. 7(a) and 7(b) is the locus of the spatiotemporal evolution of the contact line as modulated by the combined influences of the applied pressure force, the surface tension force originating from the wetted wall, the viscous drag, and the Lorentz force due to the applied magnetic field.

Since the wetting length of the advancing fluid depends on the contact line speed, we will consider this aspect in a later discussion, while elaborating the variation of contact line motion in greater detail in the next section. However, what has been observed from Fig. 7 in the present context is that we can speed up the wetting phenomenon by increasing the value of Ha for a given surface wettability corresponding to a contact angle $\theta_s = 90°$ and through careful selection of the wettability of the solid substrate for a given strength of the applied magnetic field.

From the foregoing discussion, it may be noted at this juncture that the effective capillary filling and wetting time can be controlled by varying Ha and essentially through the judicious selection of the wetting condition of the solid surface (θ_s). This observation could be of great importance in many technologically relevant areas involved with microscale transport. Also, from the inferences delineated in the above figures, we believe that the effect of magnetic field-driven alterations in interfacial dynamics can be exploited to achieve finer control of capillary filling dynamics on small scales,
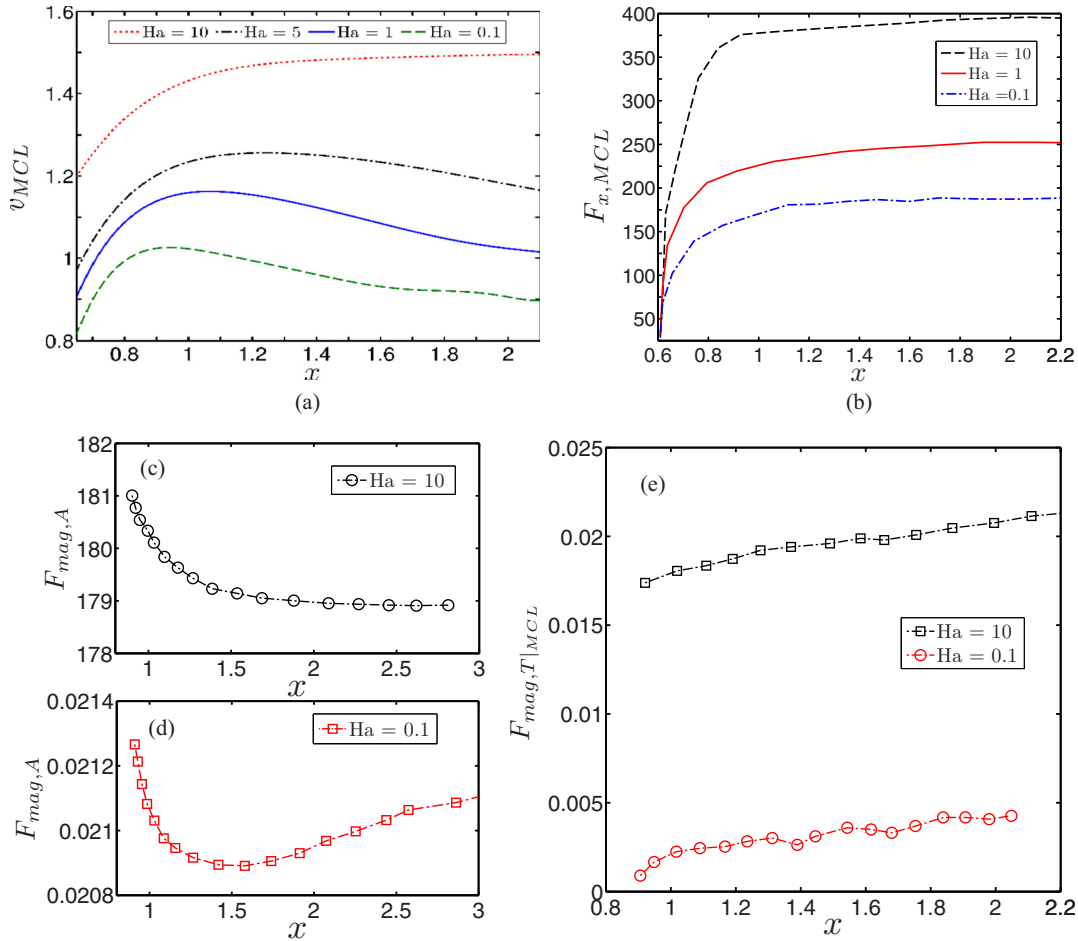
FIG. 8. (a) Plot showing the variation of contact line velocity (v_{MCL}) with distance along the length of the capillary (x) for different values of Ha = 0.1, 1, 5, and 10. The other parameters considered are Pe = 0.2, Ca = 0.08, and $\theta_s = 90°$. The velocity of the contact line is lower and higher for Ha = 0.1 and 10, respectively; (b) Variation of the net force acting over the contact line $F_{x,\mathrm{MCL}}$ with distance along the length of the capillary (x) for three different values of Ha = 0.1, 1, and 10. The net force increaases with increase in Ha. Plot depicting the variation of axial component of magnetic force ($F_{\mathrm{mag},A}$) at the channel center for different values of Ha: (c) for Ha = 10 and (d) for Ha = 0.1. The variation of transverse component of magnetic force acting at the contact line ($F_{\mathrm{mag},T}|_{\mathrm{MCL}}$) is depicted in Fig. (e) for two different values of Ha = 0.1 and 10. The following parameters are considered for plotting figures (c) and (d) as: Pe = 0.2, Ca = 0.08, and $\theta_s = 90°$.

where the capillary can be engineered in tune with the predesigned means of achieving some stated purpose.

4. Interfacial dynamics of contact line motion

We discuss here the variation of contact line motion for two different cases, viz., (i) for different values of Ha at $\theta_s = 90°$, as shown in Fig. 8(a), and (ii) for three different values of the surface wettability, $\theta_s = 45°$, $90°$, and $135°$, obtained at Ha = 1, as shown in Figs. 9(a)–9(c). It can be seen from Fig. 8(a) that the velocity of the moving contact line initially exhibits an increasing trend for all values of Ha considered. After experiencing initial acceleration, the dynamics of contact line velocity depends on the control parameters chosen. The initial increasing trend of the contact line velocity can be explained by the sudden acceleration of the binary system on application of an externally applied pressure gradient. The binary fluid system remains at rest initially but experiences a sudden jerk as the pressure gradient is applied so as to cause flow in the channel. After initial transience, the contact line has to adjust itself to the chemically homogeneous surface

and makes an attempt to maintain a "dynamic equilibrium" profile in tune with the contact angle specified over the solid substrate. Since the interface, more precisely the contact line, progresses dynamically along the channel; we have used the word "dynamic equilibrium" loosely in this context, although the contact line will never experience an equilibrium under dynamic conditions under different forcings, viz., the applied pressure force, the Lorentz force, the viscous drag, and the surface wettability

It can be inferred from Fig. 8(a) that the contact line velocity after overcoming the initial transience, continues to increase for Ha = 10, whereas for the other values of Ha (0.1, 1, and 5), it decreases as the interface moves further along the channel. Since the capillary force, for a given contact angle ($\theta_s = 90°$), remains constant, the variation observed in Fig. 8(a) for different values of Ha is mainly attributable to the effect of the Lorentz force being applied on the interface as it progresses inside the channel. Since the magnetic force, consistent with the present problem, is acting in both momentum equations (x and y momentum equations), the
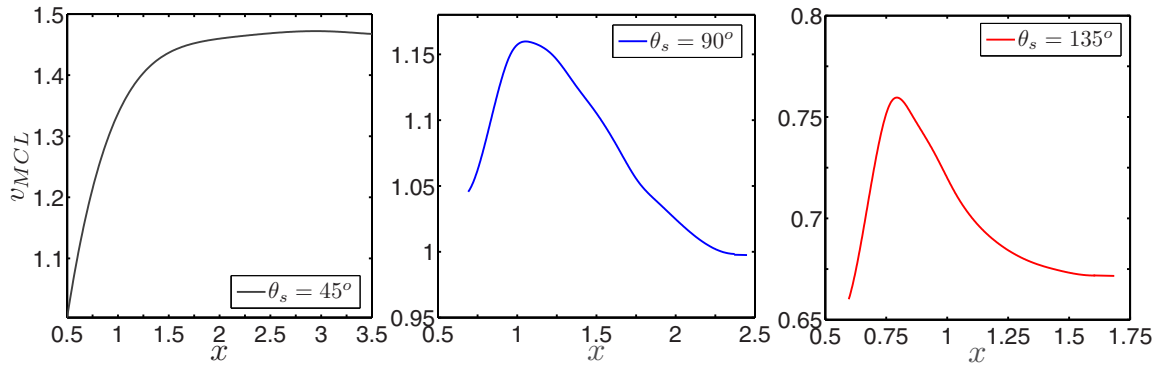
FIG. 9. Plot depicting the variation of contact line velocity (v_{MCL}) with distance along the length of the capillary (x) for three different values of $\theta_s = 45°$, $90°$, and $135°$. The other parameters considered are Pe = 0.2, Ca = 0.08, and Ha = 1. The velocity of the contact line, after overcoming the initial stage of admittance, increases for $\theta_s = 45°$, whereas for the other two values of the contact angle ($\theta_s = 90°$ and $135°$) the contact line velocity decreases. The flow still remains in the transient regime.

effect of the magnitude of the Lorentz force being applied on the contact line motion is not straightforward; rather, the gross effect of this force on the contact line depends on the interface shape and deformation, which in turn, also strongly depend on the surface wettability. We note that a higher magnitude of Ha leads to a higher contact line velocity, although it is intuitively expected that the higher value of Ha will impart a relatively higher drag to the interface at the three-phase contact line and will also reduce the velocity. However, this is not the case, as can be seen from Fig. 8(b), which shows the variation of the net force ($F_{x,\mathrm{MCL}}$) acting over the contact line as it advances along the length of the capillary. The force ($F_{x,\mathrm{MCL}}$) comprises three different forces, viz., viscous drag, the force due to applied magnetic field and the force due to presence of the interface itself in a phase field (i.e., all terms on the right-hand side of Eq. (11) except the pressure gradient).

What is observed from Fig. 8(b) is that, with an increase in Ha, the net force acting over the contact line increases, thus allowing it to move faster. To elucidate this nonintuitive phenomenon, we considered the individual contributions of the axial component ($F_{\mathrm{mag},A}$) and transverse component ($F_{\mathrm{mag},T}$) of the magnetic force-induced body force terms to the interface. The axial component magnetic body force term impedes the interface, whereas the transverse component, accounting for the mass conservation effect on the process, may aid the forward motion of the contact line, depending on the surface wettability and the magnitude of Ha being considered. In fact, for a relatively higher value of Ha (as high as 10) and for $\theta_s = 90°$, the effect of the transverse component of the body force becomes favorable [see Fig. 8(e), where the net force on the contact line is higher for Ha = 10] for the advancement of the contact line, leading to an increase in velocity of the moving contact line, as confirmed in Fig. 8(a). On the other hand, for a relatively smaller value of Ha (0.1), the retarding effect due to the axial component of the Lorentz force in the middle part of the interface also becomes smaller for smaller values of Ha as verified in Fig. 8(d). To delve deep into the retardation effect because of the axial component of magnetic force, we plot Figs. 8(c) and 8(d), which show the variation of $F_{\mathrm{mag},A}$ applied at the interface at the channel center for two different values of $Ha = 10$ and 0.1, respectively.

The variation indeed support that the retardation effect will be more pronounced for $Ha = 10$ owing to higher $F_{\mathrm{mag},A}$, leading to enhanced filling time as confirmed in Fig. 6(a). On the other hand, a relatively higher magnitude (one order higher) of $F_{\mathrm{mag},T}$ for $Ha = 10$ [see Fig. 8(e)], the net force acting at the contact line becomes higher for $Ha = 10$, thus ensuring faster wetting following a higher contact line velocity. In fact, these two effects lead to a mismatch in the motion of the different parts of the interface inside the capillary. Precisely, accounting for these cumulative effects of magnetic field-induced force components, the interface at the contact line moves slowly, while moving at a faster rate at the center of the capillary, owing to a diminished retardation effect. We have verified this in Fig. 8(a), where the velocity of the contact line reduces with decreasing value of Ha. Also, we mention here that the contact line velocity as depicted in Fig. 8(a) are in clear support with the capillary filling and capillary wetting dynamics as delineated in previous figures (Figs. 6 and 7).

We next discuss, based on Figs. 9(a)–9(c), the variation of contact line velocity for different values of the surface wettability, $\theta_s = 45°$, $90°$, and $135°$, with Ha = 1 and other parameters Pe = 0.2 and Ca = 0.08. It can be seen from Fig. 9(a) that, for $\theta_s = 45°$, the contact line velocity after the admittance of fluid-A increases and finally tends toward an asymptotic value before reaching a steady-state condition. In the cases of Figs. 9(b) and 9(c) for $\theta_s = 90°$ and $135°$, respectively, the contact line velocities show a decreasing trend after the initial stage of admittance of fluid-A and reaches asymptotic values before reaching a steady state. The flow still remains in the transient regime. Since the applied pressure force, the force due to the applied magnetic field, and the viscous drag force remain same for the given flow configuration in this study, the change in contact line velocity as observed with a change in contact angle in Figs. 9(a)–9(c) is essentially due to the surface wettability-driven alteration in the capillary force density acting at the contact line. The surface tension force consistent with $\theta_s = 45°$ favors the interface movement at the contact line, thus accelerating the contact line velocity, as can be seen in Fig. 9(a). In contrast, the surface tension force arising with $\theta_s = 135°$ makes the interface retard at the contact line, hence the contact
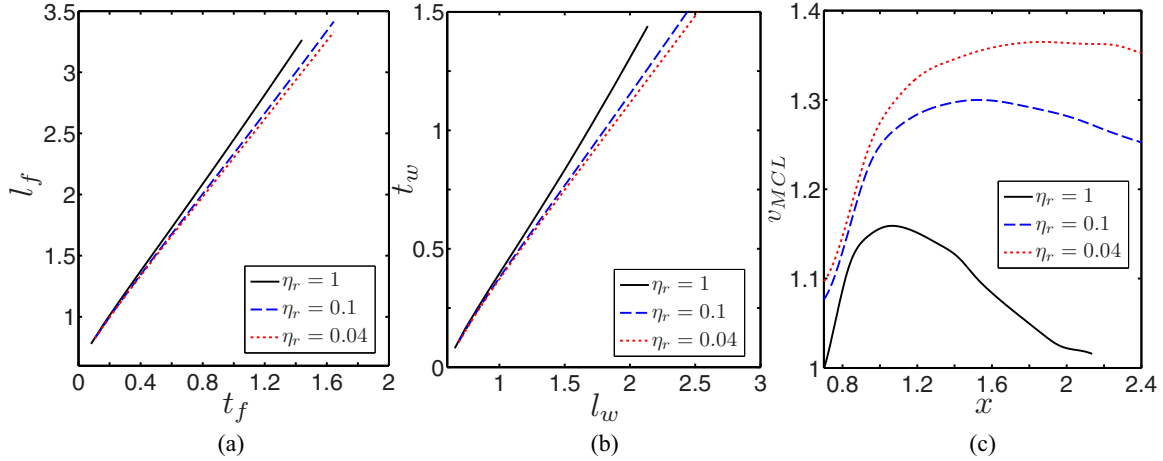
FIG. 10. Plot showing the variation of (a) capillary filling, (b) capillary wetting, and (c) the contact line velocity, obtained for three different values of the viscosity ratio, $\eta_r = 0.01$, 0.1, and 1, respectively. The other parameters for this plot are $\theta_s = 90°$, $\varepsilon_r = 1$, $\rho_r = 1$, Ha $= 1$, Pe $= 0.2$, Ca $= 0.08$, and Re $= 0.03$. With increase in viscosity of the advancing phase fluid (for a smaller value of η_r), the filling time increases and the wetting time decreases. The contact line velocity also increases with increasing viscosity of the advancing phase fluid.

line velocity decreases as the interface progresses along the channel. Although the surface tension force corresponding to $\theta_s = 90°$ does not have any assisting or opposing effect on the interface movement, the smaller magnitude of resulting force acting at the contact line ($F_{x,\text{MCL}}$) due to a relatively lower value of Ha (1) slows the contact line velocity as depicted in Fig. 9(b). We further mention here that the reduction in the velocity at the centerline has a consequential effect on the contact line movement. Thus, the results of interplay of different forcings at the three-phase contact line agree with the observations of the capillary filling and wetting dynamics as depicted in Figs. 6 and 7.

B. Effect of contrast in properties on the interfacial dynamics

1. Effect of viscosity contrast

We have investigated the effect of a contrast in viscosity on the underlying magnetohydrodynamics of binary systems as considered in this analysis. As already mentioned, we change the properties of the advancing phase fluid (fluid A) to achieve the desired contrast, leaving the properties of the fluid being displaced (fluid B) unchanged. Figures 10(a)–10(c) show the effect of viscosity contrast ($\eta_r = \eta_B/\eta_A$) on the capillary filling, capillary wetting, and contact line velocity, respectively, obtained for two different values of $\eta_r = 0.04$ and 0.1. Note that Fig. 10 also depicts the variation obtained for $\eta_r = 1$ essentially for appreciation of the effects of a viscosity contrast on the underlying transport. Figure 10 indicates that, with a decrease in η_r from a value of 1, i.e., for the cases when a relatively high-viscosity fluid displaces a less viscous fluid ($\eta_r < 1$), the filling time increases [Fig. 10(a)], whereas the wetting time decreases [Fig. 10(b)]. This contradictory behavior of the filling and wetting dynamics can be explained by the variation of contact line velocity as depicted in Fig. 10(c). Figure 10(c) indicates that, with a decrease in η_r (<1), the velocity of the contact line increases, leading to accelerated wetting dynamics, as verified in Fig. 10(b). The rapid wetting phenomenon eventually results in a longer filling

time following the effect of mass conservation in the flow field as confirmed in Fig. 10(a).

Since the dynamics of the contact line motion provides an estimate of the filling and wetting dynamics, we now consider the variation of the contact line with a change in η_r and pinpoint the effects that illustrate the disparity in the contact line motion as depicted in Fig. 10(c). In doing so, we examine the variation of viscous resistance that the contact line encounters as it moves along the channel. The viscous resistance (per unit area) being faced by the moving contact line (MCL) during its movement is given by $F_{R,\text{viscous}}|_{\text{MCL}} = \{[0.5(1 + \eta_r) + 0.5\phi(1 - \eta_r)]u_y\}$.

Figure 11(a) depicts the location of the interface at a given time $t = 1.2$ (dimensionless) for different η_r, while the inset figures show the interface contours obtained for at that instant in the computational half domain. Figure 11(b) illustrates the variation of viscous resistance for two different values of $\eta_r = 0.1$ and 0.04. The other parameters are given in the caption.

We observe a mismatch in the motion of the different parts of the interface (interface at the contact line and at the central part of the channel) with a change in η_r, with the other parameters and time remaining unchanged. A closer look at Fig. 11(a) indeed reveals that with a decrease in η_r (<1), the interface at the contact line advances, meeting a retardation effect at the channel center. These two events lead to an increase in filling time and a decrease in wetting time, as confirmed in Figs. 10(a) and 10(b). Also, Fig. 11(b), which shows the variation of the viscous resistance felt by the contact line in the process, indicates that, with a decrease in η_r (for a high-viscosity advancing phase fluid), the overall viscous drag on the contact line gradually decreases as the interface progresses along the channel. Since with time fluid B recedes from the channel, the viscous resistance offered by the receding phase fluid to the contact line decreases, culminating in reduction in overall viscous resistance. This reduction in viscous resistance leads to an enhancement of contact line velocity, which is also reflected in Fig. 10(c). We should
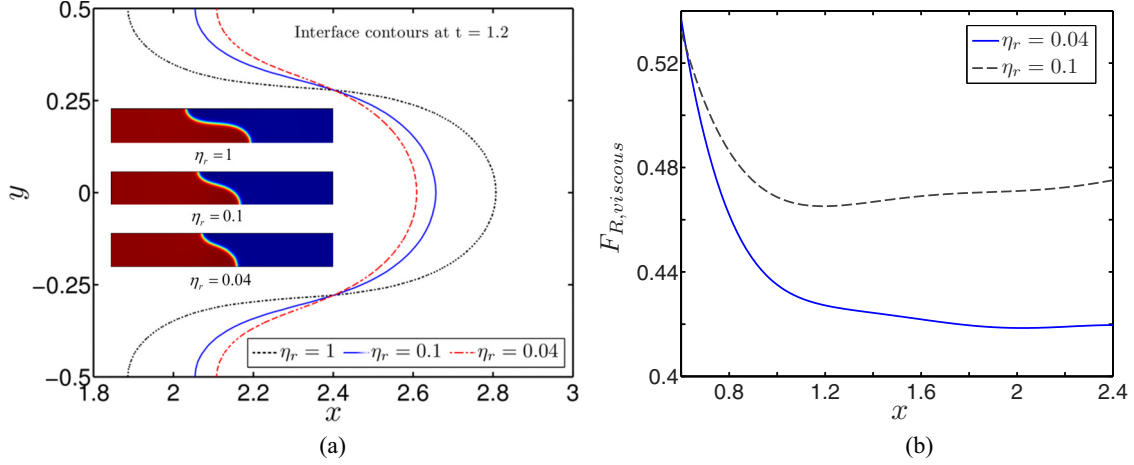
FIG. 11. (a) (Inset) Color contour plots depicting the evolution of the interface inside the channel for different values of η_r 1, 0.1 and 0.04. (Main figure) Interface contours at dimensionless time $t = 1.2$. The other parameters considered for are $\theta_s = 90°$, Ha $= 1$, $\varepsilon_r = 1$, $\rho_r = 1$, Pe $= 0.2$, Ca $= 0.08$, and Re $= 0.03$. (b) The variations of viscous drag acting at the contact line $F_{R,\text{viscous}}$ for two different $\eta_r = 0.04$ and 0.1. The other parameters considered are $\theta_s = 90°$, Ha $= 1$, Pe $= 0.2$, Ca $= 0.08$, and Re $= 0.03$.

mention that the variations in viscous resistance illustrated in Fig. 11(b) are in clear support of the contact line dynamics depicted in Fig. 10(c).

2. Effect of contrast in electrical conductivity

The conductivity ratio is an important parameter in the context of this analysis, since the magnetic forces acting over the interface largely depend on the ratio of the conductivities of the fluids in the immiscible binary system (ε_r). To obtain some insights into the effect of contrasting conductivity of the fluids (ε_r), we show the variations of filling, wetting lengths, and contact line motion for two different values of $\varepsilon_r = 0.1$ and 0.01 in Figs. 12(a)–12(c), respectively. Also, we considered the variations for $\varepsilon_r = 1$ in Figs. 12(a)–12(c) to isolate the effects of contrast in conductivity ratio on the underlying transport. The other parameters are given in the figure caption. An increase in conductivity of the advancing

phase fluid as manifested by a smaller value of ε_r (<1) leads to a delay in filling time, while speeding up the wetting phenomenon, as confirmed in Figs. 12(a) and 12(b), respectively. Figure 12(c) indicates that the contact line velocity increases in tune with a decrease in conductivity ratio ($\varepsilon_r < 1$), which, in turn, makes the wetting phenomenon faster, essentially by delaying the filling of the advancing phase fluid into the capillary.

This contradictory behavior of the wetting and filling phenomena are due to the mass conservation in the flow field. To elucidate the physical explanations behind our observations of the contact line dynamics and their consequential effects on the filling and wetting phenomena as delineated in Figs. 12(a)–12(c), we investigated in detail the underlying transport features from the perspective of the variations in magnetic field-induced force ($F_{x,\text{Mag}}|_{\text{MCL}}$) that the contact line experiences during its movement along the channel. This magnetic force can be expressed
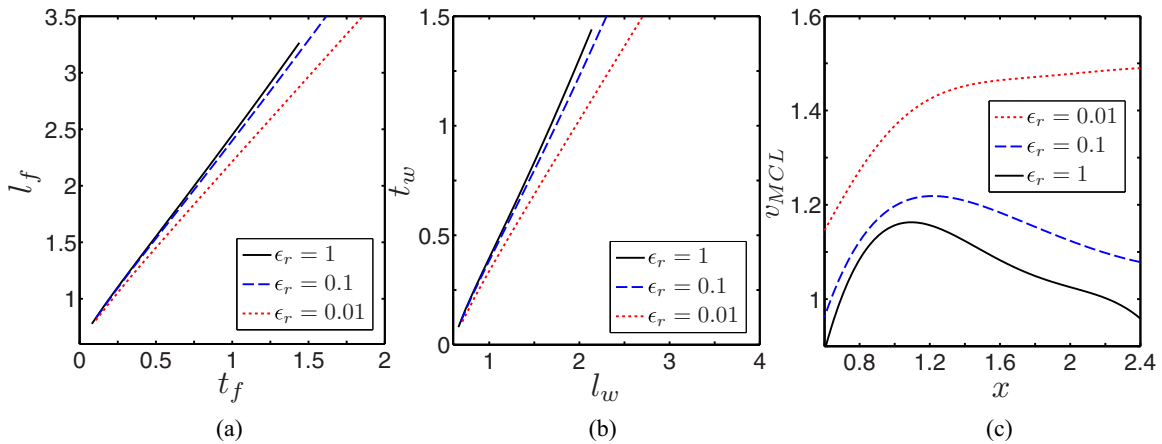

FIG. 12. Plot showing the variation of (a) capillary filling, (b) capillary wetting, and (c) the contact line velocity, obtained for three different values of conductivity ratio, $\varepsilon_r = 0.01$, 0.1, and 1, respectively. The other parameters are $\theta_s = 90°$, $\eta_r = 1$, $\rho_r = 1$, Ha $= 1$, Pe $= 0.2$, Ca $= 0.08$, and Re $= 0.03$. With an increase in viscosity of the advancing phase fluid (for a smaller value of η_r), the filling time increases and the wetting time decreases. The contact line velocity also increases with increasing viscosity of the advancing phase fluid.
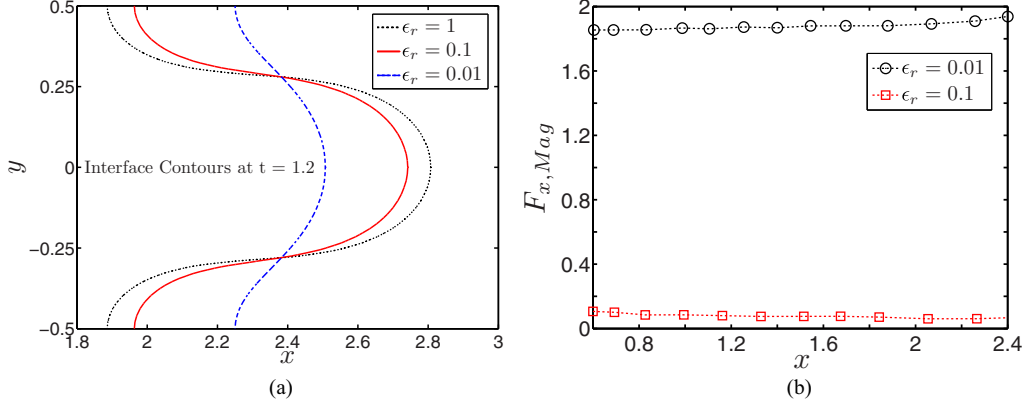
FIG. 13. (a) Plot showing the interfacial shape for different values of ε_r obtained at time $t = 1.2$ and (b) the variation of net magnetic force acting at the contact line for two values of ε_r. The other parameters are $\theta_s = 90°$, Ha = 1, $\eta_r = 1$, $\rho_r = 1$, Pe = 0.2, Ca = 0.08, and Re = 0.03. For a relatively higher conducitivity of the advancing phase fluid ($\varepsilon_r < 1$), the interface bending at the middle of the channel is higher. The magnetic force acting on the contact line becomes higher for $\varepsilon_r = 0.01$.

as $F_{x,\text{Mag}}|_{\text{MCL}} = \{\text{Ha}^2[0.5(1 + \phi)(1 - \varepsilon_r) + \varepsilon_r]u\}$. From Figs. 13(a) and 13(b), which show the deformation of the interface for different ε_r obtained at $t = 1.2$ and the net magnetic force acting over the contact line for two different values of $\varepsilon_r = 0.01$ and 0.1, respectively, we try to explain the contrasting conductivity-induced alterations in interfacial dynamics. For a relatively higher value of the electrical conductivity of the advancing phase fluid as realized through a smaller ε_r (<1) in the context of the present analysis, a weak deformation of the interface is observed in the channel [see Fig. 13(a)], whereas a larger deformation is witnessed for $\varepsilon_r = 1$.

In fact, the change in the deformation of the interface is an outcome of the variation of contact line velocity, largely stemming from the alteration in magnetic field-induced force with a change of contrast in conductivity ratio. Note that for the given set of other parameters considered, the higher the value of the advancing fluid conductivity ($\varepsilon_r < 1$), the higher is the magnetic force being applied at the contact line, albeit the strength of the imposed magnetic field remains unchanged. Figure 13(b) verifies a relatively higher magnetic force for a smaller ε_r ($= 0.01$), leading to an increased velocity of the moving contact line [see Fig. 12(c)]. This higher contact line velocity imparts a rapid wetting phenomenon, culminating in a reduction in filling rate satisfying the mass conservation in the flow field. This observation is further supported by the interface deformation as delineated in Fig. 13(a). Notably, a close look at Fig. 13(b) indicates that, with the movement of the interface along the channel, $F_{x,\text{Mag}}|_{\text{MCL}}$ increases for $\varepsilon_r = 0.01$ (a representative case of a higher conductivity of the advancing phase fluid), largely attributable to the higher momentum of the advancing phase fluid inside the channel. We should mention that the variations of $F_{x,\text{Mag}}|_{\text{MCL}}$ are in clear support of the variation of contact line velocity as depicted in Fig. 12(c).

IV. CONCLUDING REMARKS

We have investigated the capillary filling dynamics of an immiscible binary system constituted by two electrically conducting fluids under the influence of an applied magnetic field in a narrow fluidic channel. We used the energy-based

framework of the Cahn-Hilliard–Navier-Stokes system of equations with the appropriate wetting conditions to perform the numerical experimentation. We have shown how the interfacial dynamics become affected under the influence of an applied magnetic field, upon experiencing an intricate interplay among different forcings, viz., the magnetic field-induced Lorentz force, the viscous drag, and the surface tension force as modulated by the wettability of the surface. We studied the behavior of capillary dynamics under the combined influence of surface wettability and an imposed magnetic field for two different cases. First, we investigated the underlying dynamic behavior for a property-matched binary system, and in the second case, we explored the effects of contrast in properties on the underlying interfacial transport. We demonstrated that the competition among these forces causes an alteration in the net force on the interface, leading to a change in the contact line motion, which, in turn, establishes an intricate control over the capillary filling and wetting dynamics inside a narrow fluidic channel. Further, we demonstrated that a change in the ratio of the fluid properties leads to an alteration in the forcing over the interface, and its ultimate effect culminates in achieving a greater degree of controllability over the filling and wetting dynamics in the process. We believe that the results obtained from the present analysis may improve the design of microfluidic devices and systems, which are relevant to biomedical applications and products.

ACKNOWLEDGMENT

APPENDIX: COUPLING BETWEEN HYDRODYNAMICS AND THE PHASE FIELD

The coupling between the Navier-Stokes equations and the phase field is through the additional body force term $G\nabla\phi$ in the right-hand side of Eq. (5a). The expression within brackets in the free-energy functional given by Eq. (1) is known as Lagrangian, L and is a function of ϕ and $\nabla\phi$. Hence, for a 1D case, the free-energy functional can be given as

$F = \int L(x,\phi,\phi')dx$. An arbitrarily small, virtual change in this free-energy functional is given by

$$\delta F = \int \left[\frac{\partial L}{\partial \phi}\delta\phi + \frac{\partial L}{\partial \phi'}\delta\phi' \right]dx. \tag{A1}$$

Applying $\delta\phi = 0$ at boundaries and with further simplification, one arrives at the expression

$$\delta F = \int \left[\frac{\partial L}{\partial \phi} - \frac{d}{dx}\left(\frac{\partial L}{\partial \phi'} \right) \right]\delta\phi dx. \tag{A2}$$

For extremization, δF is set to zero, being true for any arbitrary $\delta\phi$. This leads to a form of Euler-Lagrange equation

$$\frac{\partial L}{\partial \phi} - \frac{\partial}{\partial x_i}\left(\frac{\partial L}{\partial (\nabla\phi)} \right) = 0. \tag{A3}$$

By Noether's theorem of calculus of variations, this can also be expressed in the form of an equivalent conservation law $\nabla \cdot \overline{\overline{T}} = 0$, where stress tensor $\overline{\overline{T}}$ is the stress due to existence of participating phases.

$$\overline{\overline{T}} = \frac{\partial L}{\partial (\nabla\phi)}\nabla\phi - L\delta_{ij}. \tag{A4}$$

This stress can be shown to take the form $G\nabla\phi$ where G is given by Eq (3). Hence, the system of equations comprising the Navier-Stokes equations in fluid dynamics and the Cahn-Hilliard phase field equation are mutually coupled through the phase field. While the Cahn-Hilliard equation takes care of the evolution of the system with the thermodynamically consistent principle of minimization of free energy, the Navier-Stokes equations take care of the hydrodynamic aspects of the flow. Under equilibrium conditions, the chemical potential G that drives the evolution of phases due to residual free energy, reduces to zero.

[1] J. C. T. Eijkel and A. van den Berg, Lab Chip **6**, 597 (2006).

[2] J. Eijkel, Lab Chip **7**, 299 (2007).

[3] R. Schoch, J. Han, and P. Renaud, Rev. Mod. Phys. **80**, 839 (2008).

[4] H. A. A. Stone, A. D. D. Stroock, and A. Ajdari, Annu. Rev. Fluid Mech. **36**, 381 (2004).

[5] T. Qian, X.-P. Wang, and P. Sheng, Phys. Rev. E **68**, 016306 (2003).

[6] A. Bandopadhyay, S. Mandal, and S. Chakraborty, Soft Matter **12**, 2056 (2016).

[7] X. Luo, X.-P. Wang, T. Qian, and P. Sheng, Solid State Commun. **139**, 623 (2006).

[8] Y. Q. Zu and S. He, Phys. Rev. E **87**, 043301 (2013).

[9] R. Verberg, C. Pooley, J. Yeomans, and A. Balazs, Phys. Rev. Lett. **93**, 184501 (2004).

[10] M. Queralt-Martín, M. Pradas, R. Rodríguez-Trujillo, M. Arundell, E. C. Poiré, and A. Hernández-Machado, Phys. Rev. Lett. **106**, 194501 (2011).

[11] H. Kusumaatmaja, C. M. Pooley, S. Girardo, D. Pisignano, and J. M. Yeomans, Phys. Rev. E **77**, 067301 (2008).

[12] P. Yue, C. Zhou, and J. Feng, J. Fluid Mech. **645**, 279 (2010).

[13] T. J. Kim and C. Hidrovo, Phys. Fluids **24**, 112003 (2012).

[14] J. Hyväluoma and J. Harting, Phys. Rev. Lett. **100**, 246001 (2008).

[15] O. Kuksenok and A. C. Balazs, Phys. D: Nonlin. Phenom. **198**, 319 (2004).

[16] O. Kuksenok, D. Jasnow, and A. Balazs, Phys. Rev. E **68**, 051505 (2003).

[17] M. Sbragaglia, R. Benzi, L. Biferale, S. Succi, and F. Toschi, Phys. Rev. Lett. **97**, 204503 (2006).

[18] U. Ghosh and S. Chakraborty, Phys. Rev. E **85**, 046304 (2012).

[19] D. DasGupta, P. K. Mondal, and S. Chakraborty, Phys. Rev. E **90**, 023011 (2014).

[20] F. Munshi and S. Chakraborty, Phys. Fluids **21**, 122003 (2009).

[21] R. Dey, D. Chakraborty, and S. Chakraborty, J. Heat Transfer **133**, 024503 (2011).

[22] S. Chakraborty and D. Paul, J. Phys. D: Appl. Phys. **39**, 5364 (2006).

[23] S. Cuevas and J. Río, Phys. Rev. E **64**, 016313 (2001).

[24] M. Rivero and S. Cuevas, Sensors Actuators B: Chem. **166-167**, 884 (2012).

[25] Y. Zhu and S. Granick, Phys. Rev. Lett. **87**, 096105 (2001).

[26] C. Cottin-Bizonne, C. Barentin, E. Charlaix, L. Bocquet, and J.-L. Barrat, Eur. Phys. J. E **15**, 427 (2004).

[27] A. Darhuber, S. Troian, and W. Reisner, Phys. Rev. E **64**, 031603 (2001).

[28] S. C. Yang, Microfluid. Nanofluidics **2**, 501 (2006).

[29] J. W. G. Tyrrell and P. Attard, Phys. Rev. Lett. **87**, 176104 (2001).

[30] P. K. Mondal, U. Ghosh, A. Bandopadhyay, D. DasGupta, and S. Chakraborty, Phys. Rev. E **88**, 023022 (2013).

[31] D. Jacqmin, J. Fluid Mech. **402**, 57 (2000).

[32] V. E. Badalassi, H. D. Ceniceros, and S. Banerjee, J. Comput. Phys. **190**, 371 (2003).

[33] J. Kim, Commun. Comput. Phys. (to be published) (2012).

[34] J. W. Cahn and J. E. Hilliard, J. Chem. Phys. **28**, 258 (1958).

[35] J. W. Cahn and J. E. Hilliard, J. Chem. Phys. **31**, 688 (1959).

[36] X.-P. Wang, T. Qian, and P. Sheng, J. Fluid Mech. **605**, 59 (2008).

[37] H. Ding and P. Spelt, Phys. Rev. E **75**, 046708 (2007).

[38] H. Abbassi and S. Ben Nassrallah, Int. Commun. Heat Mass Transf. **34**, 231 (2007).

[39] P. K. Mondal, D. DasGupta, and S. Chakraborty, Soft Matter **11**, 6692 (2015).

[40] P. Yue and J. J. Feng, J. Nonnewton. Fluid Mech. **189-190**, 8 (2012).